*Article*

# An Improved Method for Impervious Surface Mapping Incorporating Lidar Data and High-Resolution Imagery at Different Acquisition Times

**Hui Luo [1,2], Le Wang [3,*], Chen Wu [4], and Lei Zhang [5]**

[1] School of Computer Science, China University of Geosciences, Wuhan 430074, P.R. China; huiluo@cug.edu.cn
[2] Hubei Key Laboratory of Intelligent Geo-Information Processing, China University of Geosciences, Wuhan 430074, P.R. China; huiluo@cug.edu.cn
[3] Department of Geography, the State University of New York at Buffalo, Buffalo, NY 14261, USA; lewang@buffalo.edu
[4] State Key Laboratory of Information Engineering in Surveying, Mapping and Remote Sensing, Wuhan University, Wuhan 430079, P.R. China; chen.wu@whu.edu.cn
[5] School of Geodesy and Geomatics, Wuhan University, Wuhan 430079, P.R. China; zhanglei1990@whu.edu.cn
* Correspondence: lewang@buffalo.edu

**Abstract:** Impervious surface mapping with high-resolution remote sensing imagery has attracted increasing interest as it can provide detailed information for urban structure and distribution. Previous studies have suggested that the combination of LiDAR data and high-resolution imagery for impervious surface mapping performs better than using only high-resolution imagery. However, due to the high cost of the acquisition of LiDAR data, it is difficult to obtain the multi-sensor remote sensing data acquired at the same acquisition time for impervious surface mapping. Consequently, real landscape changes between multi-sensor remote sensing data at different acquisition times would lead to the error of misclassification in impervious surface mapping. This issue has mostly been neglected in previous works. Furthermore, the observation differences generated from multi-sensor data, including the problems of misregistration, missing data in LiDAR data, and shadow in high-resolution images would also challenge the final mapping result in the fusion of LiDAR data and high-resolution images. In order to conquer these problems, we propose an improved impervious surface mapping method incorporating both LiDAR data and high-resolution imagery at different acquisition times in consideration of real landscape changes and observation differences. In the proposed method, a multi-sensor change detection by supervised multivariate alteration detection is employed to obtain changed areas and misregistration areas. The no-data areas in the LiDAR data and the shadow areas in the high-resolution imagery are extracted by independent classification yielded by its corresponding single sensor data. Finally, an object-based post-classification fusion is proposed to take advantage of independent classification results with single-sensor data and the joint classification result with stacked multi-sensor data. Experiments covering the study site in Buffalo, NY, USA demonstrate that our method can accurately detect landscape changes and obviously improve the performance of impervious surface mapping.

**Keywords:** impervious surface mapping; multi-temporal data; change detection; high-resolution imagery; LiDAR; object-based post-classification fusion

## 1. Introduction

An "impervious surface" is defined as any land-cover surfaces that prevents water from infiltrating into soil, including roads, parking lots, sidewalks, rooftops, and other impermeable surfaces of the urban landscape [1]. Impervious surface has been recognized as a key environmental indicator in assessing many urban enviourment issues [1-3]. From urban hydrology aspect, increasing impervious coverage would increase the velocity and volume of urban runoff, leading to the high pressure of municipal drainage and flood prevention [4,5]. Furthermore, more nonpoint source pollution would be transported into waterway due to increased runoff coinciding with urbanization [1,6]. High percent of impervious coverage would weaken the effect of rainfall infiltration and underground water recharge [7]. Meanwhile, land surface temperature is positively related to the impervious coverage [8], which absorbs more heat [9]. Due to the facts that impervious surface has impacts on many environment aspects, it is essential to estimate urban impervious surface and monitor its variation, which plays an important role in understanding spatial extent of urban development [10].

Traditionally, reliable information about impervious surface distribution could be acquired by ground survey [5]. However, it is time-consuming and labor intensive, thus cannot provide real-time data to support city planning and development monitoring. Since remote sensing technology can provide a large-scale observation view over a long period of time[11-13], it has become an important manner to estimate impervious surface distribution timely and accurately in urban areas [14]. In previous works, coarse and moderate resolution remote sensing images were widely employed in impervious surface mapping in a regional scale by sub-pixel classifier, which could estimate the percentage of impervious coverage within one pixel [8,15-20].

For the studies in local urban areas, high spatial resolution image provides new opportunities to map impervious surface accurately in a finer scale, owing to the fact that it can offer richer spatial information including shape, texture, and context [2,5]. Many research have proven the potentials of high spatial resolution image for impervious surface mapping in urban areas [2,21-23]. However, high resolution image often suffers from the shadow problems due to the obstruction of trees and buildings in urban scene. Also, the increasing intra-class variability and decreasing inter-class variability within high resolution image leads to the difficulty in separating different land-cover classes, especially in the complex urban environment [24]. All these problems bring the challenges for the improvement of impervious surface mapping accuracy with only high resolution image [25,26].

Multi-sensor remote sensing data can provide various information from multiple physical characteristics. Thus, it shows great potentials to improve the performance for identifying the detailed impervious surface distributions by utilizing these complementary characteristics from different sources of data [27,28]. With the advent of the airborne light detection and ranging (LiDAR) technology, LiDAR data has become one of the major data sources for impervious surface mapping in complex urban environments. It can provide 3D topography information [29-33], and compensate some drawbacks of single-scene high resolution image, such as shadow effect and relief displacement [25]. Generally, LiDAR data is firstly transformed into a multi-band raster image, and then used as integrated features with high resolution multispectral image for landscape classification [34-36]. Previous studies indicated that the combination of LiDAR data and high resolution remote sensing image outperformed that using only high resolution image [24,37,38].

Nevertheless, because of the cost and technology limits for the acquisition of multi-sensor remote sensing data, it is difficult to gather LiDAR data and high resolution image covering the same area and being acquired at the same time in practical applications. In previous works, Hartfield et al. [39] used LiDAR data in 2008 and high resolution image in 2007 to map impervious surface areas based on Classification and Regression Tree (CART) Analysis for urban mosquito habitat modelling. Normalized Digital Surface Model (nDSM) extracted from LiDAR data in 2001 and aerial photograph in 2004 was combined to classify impervious surface subclasses and delineate the footprints of buildings in Downtown Houston [40]. Huang et al. [24] compare three fusion methods for 2001 LiDAR and 1999 aerial image to conduct classification in the urban areas. It can be observed that,

although many previous works mapped impervious surface with multi-temporal LiDAR data and high resolution image, they rarely consider changes and observation differences between LiDAR data and high resolution image acquired from different time. The changes and observation differences include real landscape changes, mis-registration, missing data only in LiDAR data, and shadows only in high resolution image. Since these multi-sensor data inside these areas don't provide the observation information from the same landscape, they would lead to unavoidable classification errors if they are neglected. These problems really exist in many practical applications using multi-temporal remote sensing data from different sensors.

Therefore, in order to solve these problems, the objective of this paper is to develop an improved impervious surface mapping method taking advantage of LiDAR data and high resolution remote sensing image from different acquisition time. Specifically, the proposed method combines automatic change detection and object-based post-classification fusion for multi-temporal LiDAR data and high resolution image, which means that these two different sensor data are acquired in different time respectively.The more recent data (LiDAR data or high resolution image) is used as the target data for mapping the impervious surface distribution at that time. While the other sensor data (high resolution image or LiDAR data) acquired at an earlier time is utilized as auxiliary data involved in this impervious surface mapping. In the first step, the stacked multi-temporal data (LiDAR data and high resolution image) is segmented into objects with multi-resolution segmentation (MRS) [41] to maintain the completeness of landscape object and avoid 'salt and pepper' noise. Then, supervised multivariate alteration detection (MAD) [42-44] and OTSU thresholding method [45] are applied to detect changes between multi-temporal LiDAR data and high resolution image, including real landscape changes, and mis-registration of buildings due to different observation angles. Other observation differences, including no-data areas in LiDAR data and shadow areas in the high resolution image, are extracted from independent classification yielded by the corresponding single sensor data (LiDAR data or high resolution image). Finally, the impervious surface map is accurately generated by the proposed object-based post-classification fusion integrating the joint classification result (generated by multi-sensor data: LiDAR data and high resolution image) with the independent classification results, according to the extracted changed areas and observation difference areas. More importantly, the spatial information from segmentation object map is employed for a more complete and accurate mapping result during the fusion stage.

In this paper, we have two main contributions: 1) change detection for real landscape changes with multi-temporal multi-sensor data by multivariate alteration detection (MAD); 2) more importantly, impervious surface mapping by the proposed object-based post-classification fusion combining joint classification results with stacked multi-sensor data and independent classification results with single sensor data.

The paper is structured as follows. Section 2 provides the information of study site and data. In Section 3, the methodology used to achieve the above goal is presented. Section 4 follows with the description and analysis of the experiment. The discussion is shown in Section 5. And finally, Section 6 draws the conclusion.

## 2. Study Site and Data Description

### *2.1. Study Site*

The study site was near the boundary of downtown area in Buffalo, NY, USA, which is shown in Figure 1. The center of this study site image is located at 42°52' 53.16" N and 78°51' 45.02" W. Land cover of this area was dominated by impervious surface, including residential and commercial buildings, road, pavements, and parking lots, together with large areas of vegetation (trees and grass) and small areas of bare soil. The study site is typical urban areas in the USA, which makes it ideal for this study.

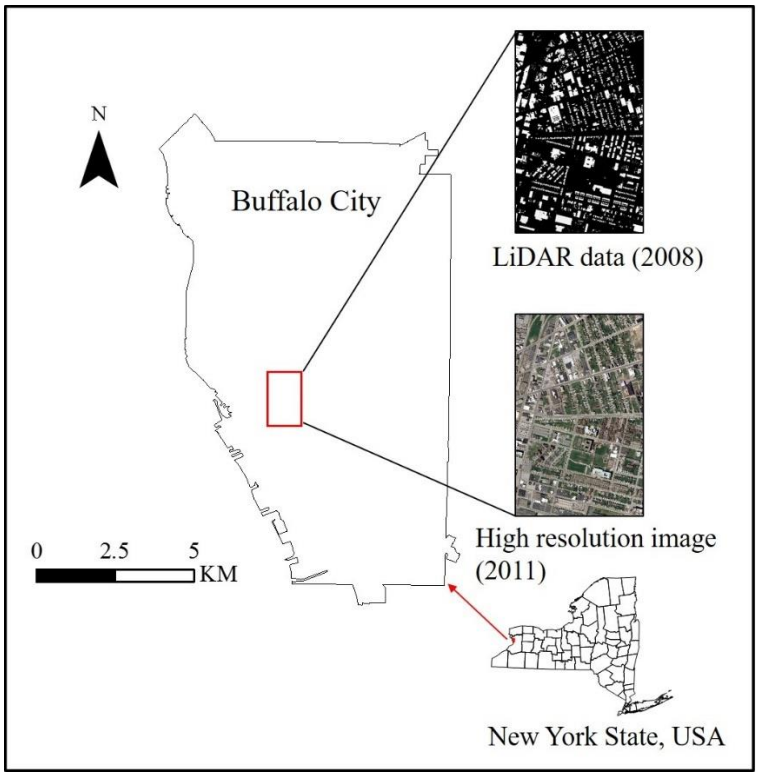


**Figure 1.** Study site: Buffalo, NY, USA

*2.2 Data*

1. High resolution image

In this paper, the high resolution digital aerial orthoimage in the year of 2011 provided by the New York State Digital Orthoimagery Program (DYSDOP) (can be downloaded in the website of NYSGIS Clearinghouse) was used in the experiment. It contains four bands, which are red band, green band, blue band, and near-infrared band. The resolution of this optical high resolution image is 0.3048 meter (1 foot). The orthoimages covering the study site were mosaiced and relative radiometric corrected using ArcGIS 10.1™ into a test image, which is shown in Figure 1.

2. LiDAR data

The airborne LiDAR data were acquired in summer 2008 with average point spacing of 0.956 meter. The LiDAR point data was saved as LAS format 1.0, which has been classified into ground pixel and non-ground pixel with Terrascan™. All the raster images were generalized by binning interpolation type with natural neighbor void fill method available in LAS Dataset to Raster Tool of ArcGIS 10.1™, as shown in Figure 1. There are two bands in the LiDAR data, including nDSM and intensity. All elevation points of the first return in LAS files were interpolated into 1-meter resolution nDSM. The intensity raster of landscape surface was acquired by the first return of LAS Files with 1 meter resolution. There are some no-data areas resulting from no laser beam returned because of the obstruction of tall buildings or the absorption of materials. The no-data areas in the LiDAR data are generally shown in black color in the corresponding figures.

*2.3 Changes and Observation differences between multi-temporal LiDAR data and high resolution image*

There are numerous changes and observation differences between multi-temporal LiDAR data and high resolution image, which include real landscape changes, mis-registration, no-data areas in the LiDAR data and shadows in the high resolution image, which are shown in Figure 2. The real landscape change between these two different sensor data acquired at different time is shown in Figure 2 (a) and (b). Specifically, the idle areas from LiDAR data acquired in the 2008 is built to be houses in the high resolution image acquired in the 2011. Figure 2 (c) and (d) indicates that, although geometry correction for multi-temporal LiDAR and high resolution image was conducted, some mis-registration of high buildings still

exist, since the imaging mode of two sensors are different and orthorectification error (orthorectification cannot solve all the problems of observation angle for high buildings) is unavoidable in the high resolution image. Some special materials of land surface or building roof may absorb the laser wave emitted from LiDAR sensor, leading to the missing data problems in the LiDAR raster image, which is shown in Figure 2 (f). But these no data areas having valid data in the high resolution image, as shown in Figure 2 (e). Because the high resolution image belongs to the optical imagery, shadows are unavoidable while they are not a problem in the LiDAR data, which is shown in the Figure 2 (g) and (h).

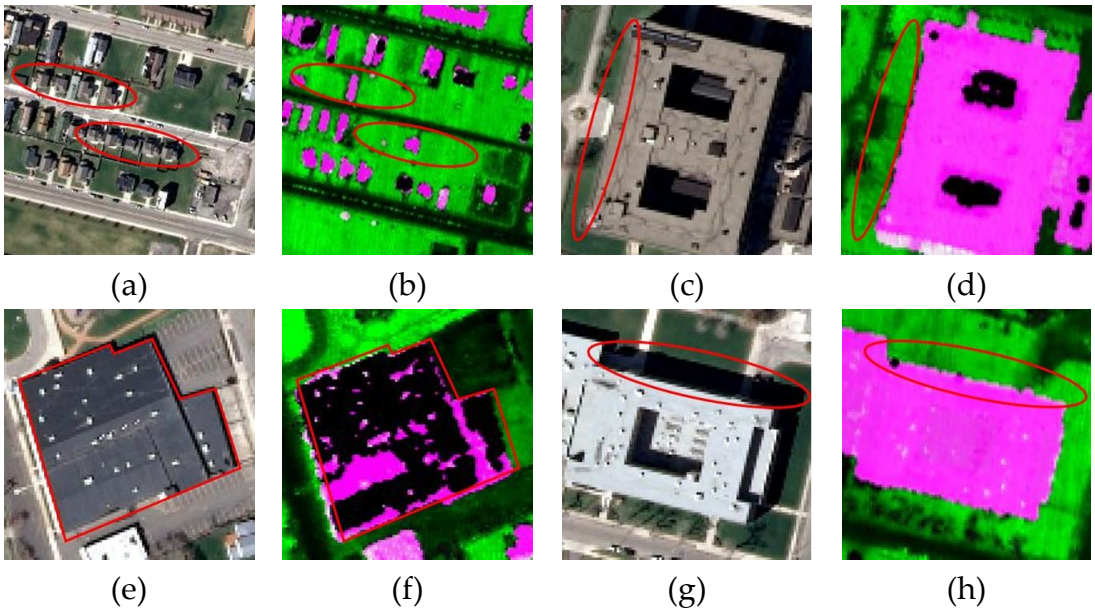


**Figure 2.** The changes and observation difference between multi-temporal high resolution image and LiDAR data are highlighted in the red circle or polygon, and all the LiDAR data is displayed in pseudo color raster image (red band and blue band: nDSM, green band: intensity), including (a) high resolution image after changes; (b) LiDAR data before changes; (c) high building in high resolution image with mis-registration; (d) high building in LiDAR data with mis-registration; (e) high resolution image without missing data ; (f) LiDAR data with missing data; and (g) high resolution image with shadows; (h) LiDAR data without shadows .

### *2.4 Pre-processing*

In order to integrate the high resolution image and LiDAR data, the high resolution image was firstly down-sampled from 0.3048 meter (1 foot) to 1 meter resolution. The size of the study site images is 1701×1070 $m^2$. All feature bands in high resolution image and LiDAR data were normalized in the range of 0-255. The ground and non-ground were assigned as 0 and 255, respectively. Although the multi-temporal data were both geo-referenced, there are still some mis-registrations. Accurate co-registration was performed with manually selected GCPs. However, due to the different observation angles, it is impossible to make a perfect registration for high buildings. The residual mis-registration will be processed in the proposed fusion method.

## 3. Methodology

In this section, we will introduce the details of the proposed method. Most procedures of the proposed method are coded by the MATLAB™ platform, while the segmentation step was conducted by the eCognition Developer™.

### *3.1 Segmentation*

Object-based process is very effective in the analysis and interpretation of high resolution remote sensing data. Thus, we employ segmentation to produce homogeneous objects as the basic units. MRS is one of the most popular and effective segmentation algorithms. The algorithm is a bottom-up

Peer-reviewed version available at Remote Sens. 2018, 10, 1349; doi:10.3390/rs10091349



region merging technique to form homogenous objects starting with single pixels [41]. The commercial software of eCognition Developer™ embedded this algorithm is employed in this study.

Except for the segmentation with single sensor data (high resolution image or LiDAR data) involved in independent classification step, segmentation object map produced with stacked LiDAR data and high resolution image is also employed in both change detection and post-classification step. Specifically, the objects are formed according to the information from stacked dataset, thus the pixels within one object are temporally similar, which means that they are all changed or unchanged. Therefore, the changed areas can be divided as independent objects, and would not be mixed with the unchanged areas. After segmentation, the feature value of one object is assigned as the mean value of all pixels inside.

*3.2 Change detection*

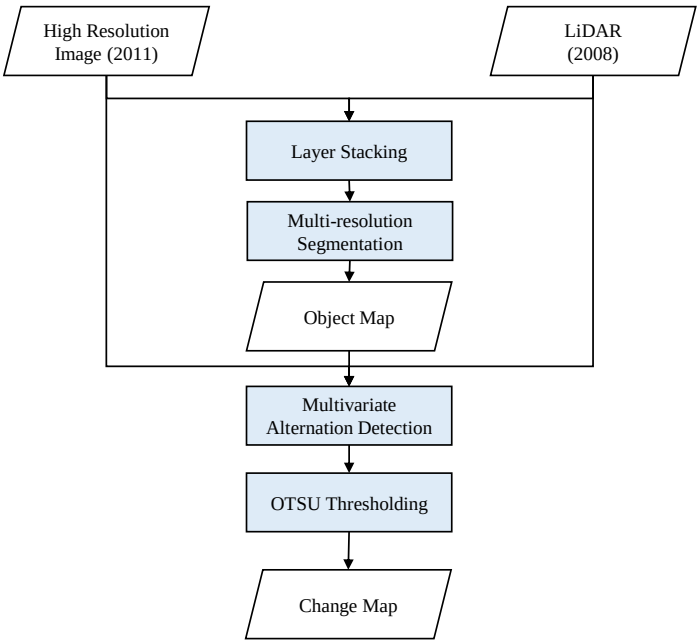


**Figure 3.** Flowchart of change detection with multi-temporal LiDAR data and high resolution image

In most previous studies, the high resolution image is integrated with LiDAR data directly, since they are all under the assumption that the multi-sensor data provide the information of the same landscape. However, when the multi-sensor data are acquired at different time, there will be numerous changes and observation differences spread over the whole image [46,47], which have been described in detail in section 2. If these changes and observation differences are neglected, the misclassification errors will be unavoidable, since the features of the corresponding areas are provided by different landscapes. Therefore, change detection between multi-temporal data was employed to distinguish the changed areas and mis-registration areas. While the shadow areas are extracted by classification from high resolution image, and no-data areas are detected by thresholding to LiDAR data.

Since the feature bands of different sensor data are acquired by different observation mechanisms, post-classification is the most straightforward method to detect changes. Namely, changed areas are detected directly through comparing the two independent classification results, which are acquired from the corresponding sensor data, respectively. However, the accuracy of post-classification is mostly unsatisfactory since the classification with only single sensor data is hard to get good performance and the classification error will be accumulated [48-50]. It is worth noting that although feature bands are not same, there will be correlations between data from two different sensors for the same landscape. For example, grass with specific spectral signature will show low elevation and high intensity in LiDAR data, while building with another spectral signature will have high elevation and low intensity. Therefore, the idea for direct change detection between multi-

temporal and multi sensor data is to find the correlations between different features, and detect the anomalous changed objects.

We employ MAD algorithm to detect the changes between multi-temporal LiDAR data and high resolution image. The procedure of change detection is shown in Figure 3. The stacked dataset is firstly segmented to object maps by MRS, which has been introduced in the previous section. After segmentation, object is the basic unit of the feature band, whose value was assigned as the mean of pixels within one object. And then MAD algorithm is employed to extract change information. Finally, OTSU thresholding method is used to separate the changed areas.

MAD derives from canonical correlation analysis, and wants to find the transformed features maximizing the variance of their difference. Mathematically, for two multi-temporal data **X** and **Y**, MAD wants to find transformation vector $\boldsymbol{a}$ and $\boldsymbol{b}$, so that:

$$\arg\max_{\boldsymbol{a},\boldsymbol{b}} \left\{ \mathrm{Var}\left( \boldsymbol{a}^{\mathrm{T}}\mathbf{X} - \boldsymbol{b}^{\mathrm{T}}\mathbf{Y} \right) \right\} \quad (1)$$

under the constraints that $\mathrm{Var}\left(\boldsymbol{a}^{\mathrm{T}}\mathbf{X}\right)=1$ and $\mathrm{Var}\left(\boldsymbol{b}^{\mathrm{T}}\mathbf{Y}\right)=1$.

It can be observed from Equation (1) that since the transformed vector for each data is different, MAD can deal with multi-sensor data and find the transformation feature space to analyze their correlation.

The optimization objective can be transformed into the following equation:

$$\mathrm{Var}\left( \boldsymbol{a}^{\mathrm{T}}\mathbf{X} - \boldsymbol{b}^{\mathrm{T}}\mathbf{Y} \right) = 2\left\{ 1 - \mathrm{Cor}\left( \boldsymbol{a}^{\mathrm{T}}\mathbf{X},\ \boldsymbol{b}^{\mathrm{T}}\mathbf{Y} \right) \right\} \quad (2)$$

where maximizing the variance equals to minimizing the correlation. And this optimization problem can be solved by calculating two generalized eigenvalue problems:

$$\boldsymbol{\Sigma}_{\mathbf{XY}}\boldsymbol{\Sigma}_{\mathbf{YY}}^{-1}\boldsymbol{\Sigma}_{\mathbf{YX}}\boldsymbol{a} = \rho^2\boldsymbol{\Sigma}_{\mathbf{XX}}\boldsymbol{a} \quad (3)$$

$$\boldsymbol{\Sigma}_{\mathbf{YX}}\boldsymbol{\Sigma}_{\mathbf{XX}}^{-1}\boldsymbol{\Sigma}_{\mathbf{XY}}\boldsymbol{b} = \rho^2\boldsymbol{\Sigma}_{\mathbf{YY}}\boldsymbol{b} \quad (4)$$

where $\boldsymbol{\Sigma}_{\mathbf{XX}}$, $\boldsymbol{\Sigma}_{\mathbf{YY}}$ and $\boldsymbol{\Sigma}_{\mathbf{XY}}$ are the covariance matrix of data **X**, data **Y** and their interaction. After the transformation vectors are obtained, the difference of transformed features is used to detect changes.

The best change detection performance will be obtained by the transformed features with the maximum eigenvalue that aim at finding the maximum correlation between multi-temporal data. There must be some correlations between different features generated from different sensor image for the same landscape, while the real changes should be anomalous from this correlation. Therefore, the MAD transformed features will minimize the difference of observation features by maximize the correlation of the unchanged landscapes. In this way, the real changes will be highlighted. So, in our experiment, the last MAD transformed feature corresponding to the maximum eigenvalue was selected to distinguish changed areas.

Although the unsupervised MAD can analyze the correlation of the whole data, the feature learning may be affected by changed areas. Training samples are necessary to classify different landscape classes. Thus, training samples from the unchanged areas in multi-temporal LiDAR data and high resolution image can be used for transformation space learning. Then, the transformed features of the whole data are calculated with the learned transformation vectors.

The difference of features corresponding to the maximum correlation is used to detect changes. Finally, the binary change map is automatically obtained by applying OTSU thresholding method on the absolute difference image of the last MAD features.

### *3.3 Object-based post-classification fusion*

After change detection, the LiDAR data and high resolution image from different acquisition time are integrated to map the impervious surface distribution considering the changes and

observation differences. In order to get a better fusion performance, an object-based post-classification fusion method (containing three main fusion steps) is proposed by considering the spatial information from object map, which integrates the joint classification result for stacked multi-sensor data with the independent classification result for single sensor data.

Generally, in most traditional processes for the fusion of different types of data, some change areas or observation difference areas, such as shadows [51], in one independent classification result yielded by the corresponding single image is directly filled with another independent classification results. However, it will not get a good performance, since independent classification with only single data is not very effective when dealing with the complex urban environment. Therefore, we propose a new object-based post-classification fusion method to solve the problems of real landscape changes and observation differences between multi-temporal LiDAR data and high resolution image by considering the spatial information from object maps. It is worth noting that for the changed areas and observation difference areas, they only appear in one image, not in both of the multi-temporal data. For example, the no-data areas are only contained in the LiDAR data, while the high resolution image can provide the hidden information inside these areas; the shadow areas only appear in the high resolution image, while the LiDAR data can show the detailed landscapes under shadows; for the changed areas, the landscape class in the latest target data reflects the impervious surface mapping result at that time. So, the core idea of the object-based post-classification fusion is to take advantage of joint classification results located in the neighbors of changed and observation difference areas as much as possible, according to the object spatial information.

Using the fusion for changed areas as an example in Figure 4, we regard the newly acquired high resolution image (the year of 2011) as the target image. Since the target image is newer and its landscape is more accurate, the object map $M_1$ is generated by the target image, which is used as the main input data in the fusion for changed areas part. Generally, all the homogenous pixels within one object belongs to the same class of landscape, which is employed as the core concept for the illustration of the post-classification fusion procedure below. Besides, the change map between multi-temporal LiDAR data and high resolution image is obtained by the method provided in the Section 3.2. For an object in the $M_1$, 1) if it is totally in the interior of the changed areas, its class can only be determined according to the independent classification result from the high resolution image; 2) if this object is intersected with the changed areas, it means that the class type of this object should be consistent with the class type of the intersection areas between this object and unchanged areas. Pervious research show that joint classification with stacked LiDAR data and high resolution image generally has a better performance than the independent classification result yielded by sole sensor data [37]. Thus, the class type of this object is determined by the class extracted from joint classification result located in the intersection between unchanged areas and this object. Ultimately, the object spatial information is used in this way during the class identification of the changed areas. Similarly, the fusion for no-data areas, shadows and mis-registration can be conducted according to nearly the same idea above, whereas the inputs object map and independent classification map are different from these two maps involved in the Figure 4. The specific input maps of the fusion for no-data areas, shadows and mis-registration is displayed in the Figure 5.

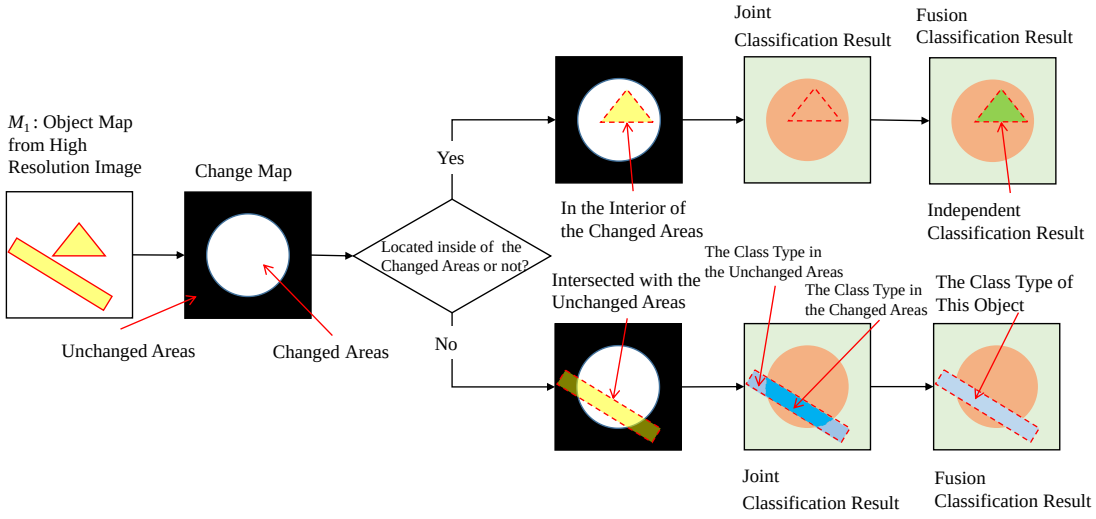


**Figure 4.** diagram for the object-based post-classification fusion

In summary, the procedure of the object-based post-classification fusion is shown in Figure 5, and described as follows in detail. Firstly, MRS was used to generate three object maps with high resolution image, LiDAR data, and the stacked dataset, respectively. After object maps were acquired, seven features (mean, variance, shape index, length-width ratio, density and roundness) [52] of each object were calculated as the input of the next classification step. Except the seven features, NDVI was also involved in the independent classification with high resolution image. Secondly, the stacked dataset of LiDAR data and high resolution image is classified to get the joint classification map, and the independent classification maps are also obtained with the corresponding single sensor data. The same training samples are used in the three classification processes, and the shadow class is not included only in the classification of LiDAR data. Support vector machine (SVM) with Gaussian kernel is chosen as classifier in this study due to its significant performance dealing with small samples [53]. Thirdly, the final classification result for the newer sensor data (high resolution image acquired in the year of 2011) was produced through three steps of the object-based post-classification fusion with three classification results (one joint classification and two independent classifications), including the fusion for the no-data areas of LiDAR data, the real changed areas between LiDAR data and high resolution image resulted from different acquisition time, and the shadow areas of high resolution image. Finally, the impervious surface map at newer time (the year of 2011) was obtained by class merging with the final classification result.

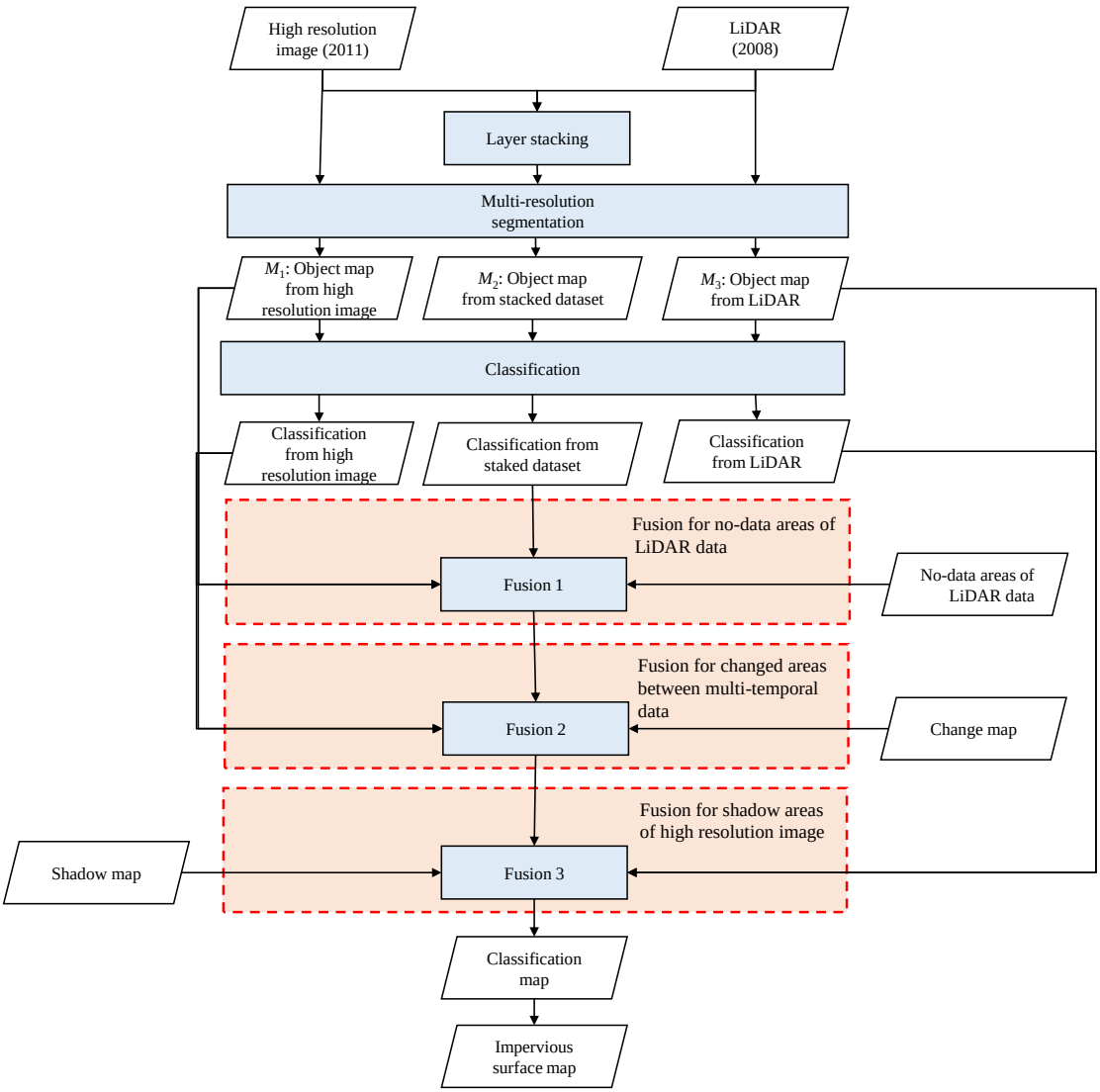


**Figure 5.** Flowchart of object-based post-classification fusion with multi-temporal LiDAR data and high resolution image

The details of the three main fusion steps involved in the Figure 5 are described as follows:

3. Fusion for no-data areas of LiDAR data

There are some no-data areas in the LiDAR data as shown in Figure 6 (b), which would lead to the classification errors. So, the first step of the object-based post-classification fusion is to acquire the correct classification result for the no-data areas in LiDAR data. The no-data map of LiDAR data was generated by thresholding. Specifically, the object map from high resolution image was employed, since high resolution image can provide the accurate object spatial information for these no-data areas. It can be seen in Figure 6, although there are some no-data areas in the LiDAR (Figure 6 (b)), they should be inside a building object according to the object map from high resolution image (Figure 6 (a) and (c)), and the whole building object will belong to the same class type. Therefore, in the object-based post-classification process, we select an object, which intersect with the no-data areas of LiDAR data. The final classification result of the selected object is conducted by major vote from the class types (extracted from joint classification result) of all the pixels, whose value in the LiDAR data is positive and also located in this object. But if all the pixels within the selected object have no data in LiDAR data, the class type of this object is determined by the independent classification with only high resolution image.

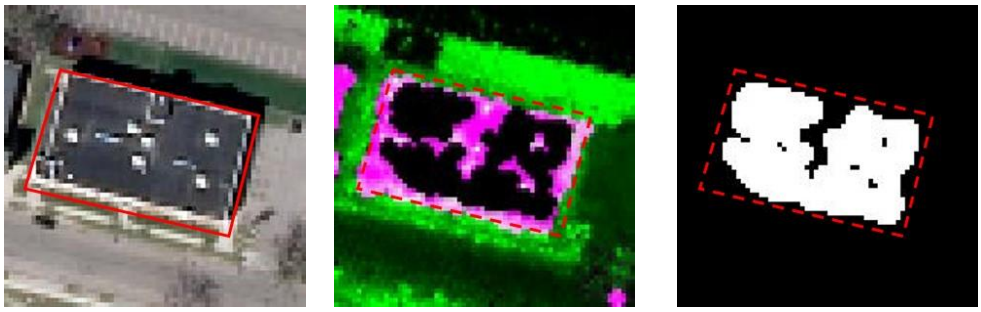

(a) (b) (c)

**Figure 6.** The spatial correspondence for the no-data area between multi-temporal LiDAR data and high resolution image, which are: (a) high resolution image; (b) LiDAR data; and (c) mask for no-data area. The red rectangle indicates the schematic object from the high resolution image.

## 4. Fusion for changed areas between multi-temporal LiDAR data and high resolution image

Since the high resolution image was acquired later than LiDAR data, we use the high resolution image as the target image to obtain the latest impervious surface map. The change map (involving mis-registration areas) is obtained by the proposed change detection method in section 3.2. The object map $M_1$ of the high resolution image is utilized for the purpose of considering the spatial and shape compactness of landscape distribution, as shown in Figure 7. According to the detailed text described about Figure 4 above, if one object from $M_1$ is located inside of the changed areas, the final class type should be assigned according to the independent classification result from high resolution image. While for the unchanged areas, the class type is assigned according to the joint classification result. In addition, if the object has the intersection with both changed area and unchanged areas, the class type of this object will be determined by the major vote of the joint classification results in unchanged areas. It is because one object should be homogenous and belong to only one class of landscape. Besides the real landscape changes, the mis-registration areas are also a type of change, technically. So, mis-registration areas can also be detected by change detection, and its correction is also completed after this fusion step, as shown in Figure 8.

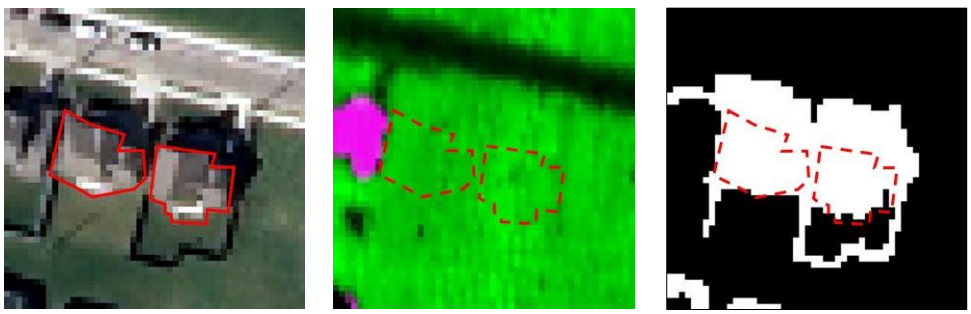

(a) (b) (c)

**Figure 7.** the spatial correspondence for the changed areas between multi-temporal LiDAR data and high resolution image, which are: (a) high resolution image; (b) LiDAR data; and (c) mask for changed area. The red rectangle indicates the schematic object from the high resolution image.

Peer-reviewed version available at Remote Sens. 2018, 10, 1349; doi:10.3390/rs10091349



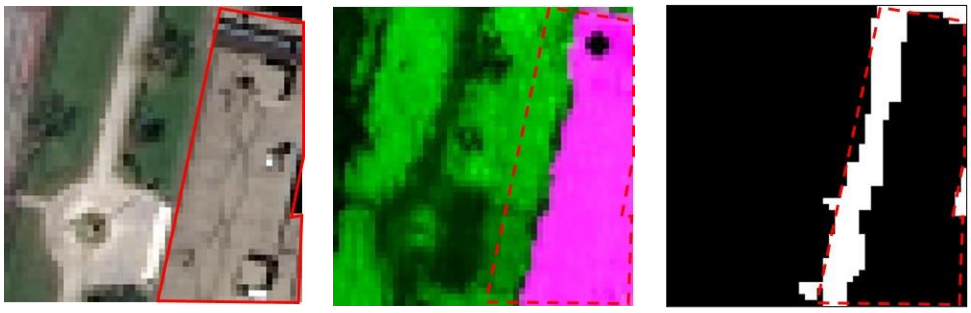

(a) (b) (c)

**Figure 8.** the spatial correspondence for the mis-registration areas between multi-temporal LiDAR data and high resolution image, which are: (a) high resolution image; (b) LiDAR data; and (c) mask for no-data area. The red rectangle indicates the schematic object from the high resolution image.

## 5. Fusion for shadow areas of high resolution image

For determining the landscape class under the shadow areas with LiDAR data and high resolution image, a direct method is to use the independent classification result from LiDAR data to restore the class information. However, as we discussed above, the independent classification is not as accurate as the joint classification. Therefore, we take advantage of the spatial object information from LiDAR data by the proposed object-based post-classification fusion. As shown in Figure 9, there is no shadow problems for LiDAR data in the same area of high resolution image. According to the object map $M_3$ from LiDAR data, the landscape under the shadows is generally related with the landscape near the shadow and belongs to the same class. Specifically, if shadow area and none shadow area are both exist in an object, the class type of landscape under shadow areas is determined by the results computed by the major vote among all the class types (extracted from joint classification) in the none shadow areas. If the object is completely located within the shadow areas, the class of this object is determined by the independent classification result with only LiDAR data. The shadow map used in this process is obtained from the independent classification of high resolution image.

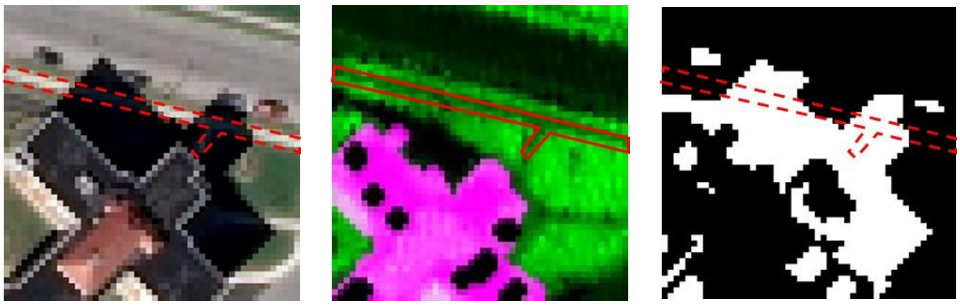

(a) (b) (c)

**Figure 9.** the spatial correspondence for the shadow areas between multi-temporal LiDAR data and high resolution image, which are: (a) high resolution image; (b) LiDAR data; and (c) mask for shadow areas. The red rectangle indicates the schematic object from the LiDAR data.

It can be seen that all these three steps all utilize the similar core concept of proposed object-based post-classification fusion. After the above three steps of the proposed object-based post-classification fusion, the final classification result is acquired, considering the differences between LiDAR data and high resolution image from different acquisition time, and taking advantage of many

Peer-reviewed version available at Remote Sens. 2018, 10, 1349; doi:10.3390/rs10091349



features from different sensor data. The latest impervious surface map is generated by class merging based on the final classification.

## 4. Experiment

### *4.1 Change detection*

The high resolution image and LiDAR data were stacked, and segmented by MRS algorithm with the eCognition DeveloperTM. The segmentation parameters are set on the basis of visual interpretation to maintain the completeness of landscape objects, where scale is 20, weight of shape is 0.1, and weight of compactness is 0.5.

The training samples are selected manually for both change detection and classification, which contains 114 pixels for roof, 97 pixels for vegetation, 80 pixels for road and parking lots, 79 pixels for soil, 98 pixels for pavement, and 93 pixels for shadow. In the change detection, the five classes of training samples except shadow are used for training.

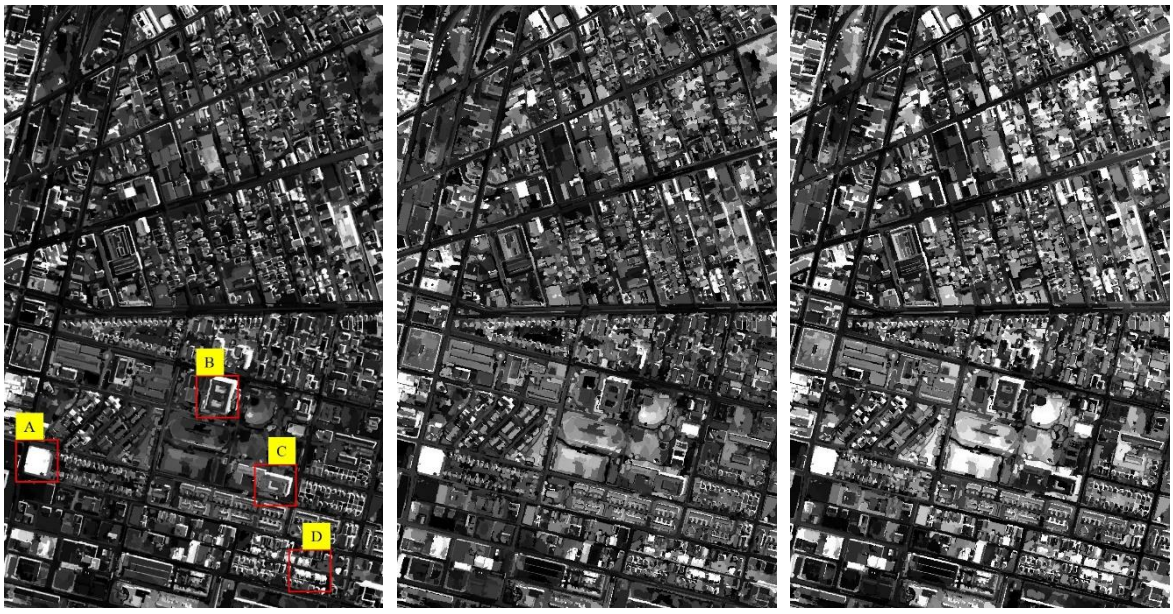


**Figure 10.** Change intensity images obtained by (a) supervised MAD, (b) unsupervised MAD, and (c) stack PCA.

In this experiment, except for the proposed supervised MAD method (sp_MAD), we also use unsupervised MAD (un_MAD), stack PCA (st_PCA) [54] and post-classification (post-class) [47,55] for comparison. Unsupervised MAD was used on the whole image to extract the correlation between multi-temporal data. PCA transformation was applied on the stacked dataset, and the change information was found in the 4th Principal Components (PCs). This is because the information of unchanged areas with major proportion can be concentrated in the top PCs, thus change information is highlighted in one of the rest bands. However, the disadvantage of stacked PCA method is that it's hard to determine which band is useful for change detection. In this paper, the change information band of stack PCA is determined by visual interpretation. Post-classification is a classical method for change detection, that directly compare class type of two independent classification results produced from the corresponding single sensor data. If the class type from these two classification results are different, it means that change phenomenon exists, and vice versa.

Peer-reviewed version available at Remote Sens. 2018, 10, 1349; doi:10.3390/rs10091349



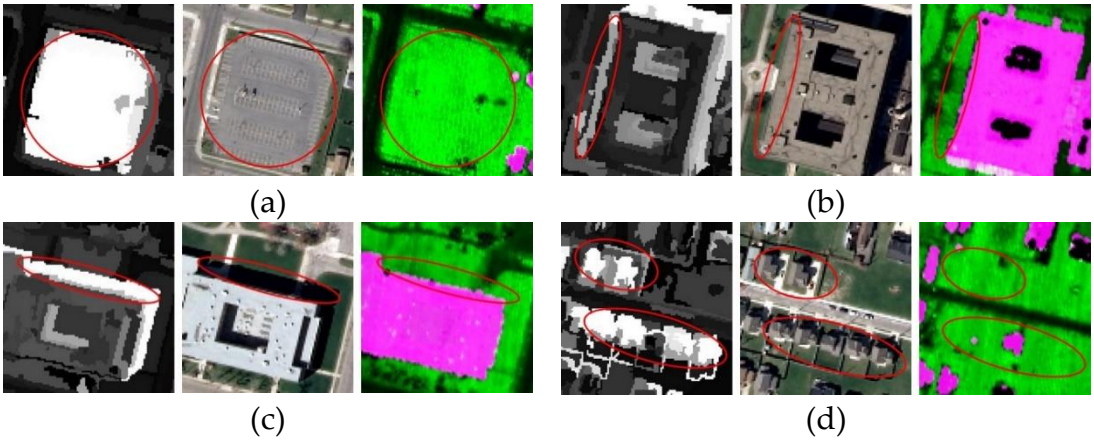


**Figure 11.** The change intensity image of supervised MAD (grey scale image), and its corresponding areas in high resolution image (true color image) and LiDAR data (pseudo color image), which are in the cases of (a) real landscape change, (b) mis-registration, (c) shadows, and (d) real landscape change.

The change intensity images of supervised MAD, unsupervised MAD and stacked PCA are shown in Figure 10, which include the absolute values of feature bands with change information. High value indicates high possibility for change. For better illustration the changes detected in the change intensity image, the change intensity image of supervised MAD, and its corresponding areas in high resolution image and LiDAR data are shown in Figure 11, which are (a) real landscape change, (b) mis-registration, (c) shadows, and (d) real landscape change. By combing Figure 10 and Figure 11, it can be observed that the proposed supervised MAD method has the ability to detect the changes and some observation differences in multi-temporal LiDAR data and high resolution image. In the visual comparison, the areas with data change are better highlighted in the result of supervised MAD than the other two methods.

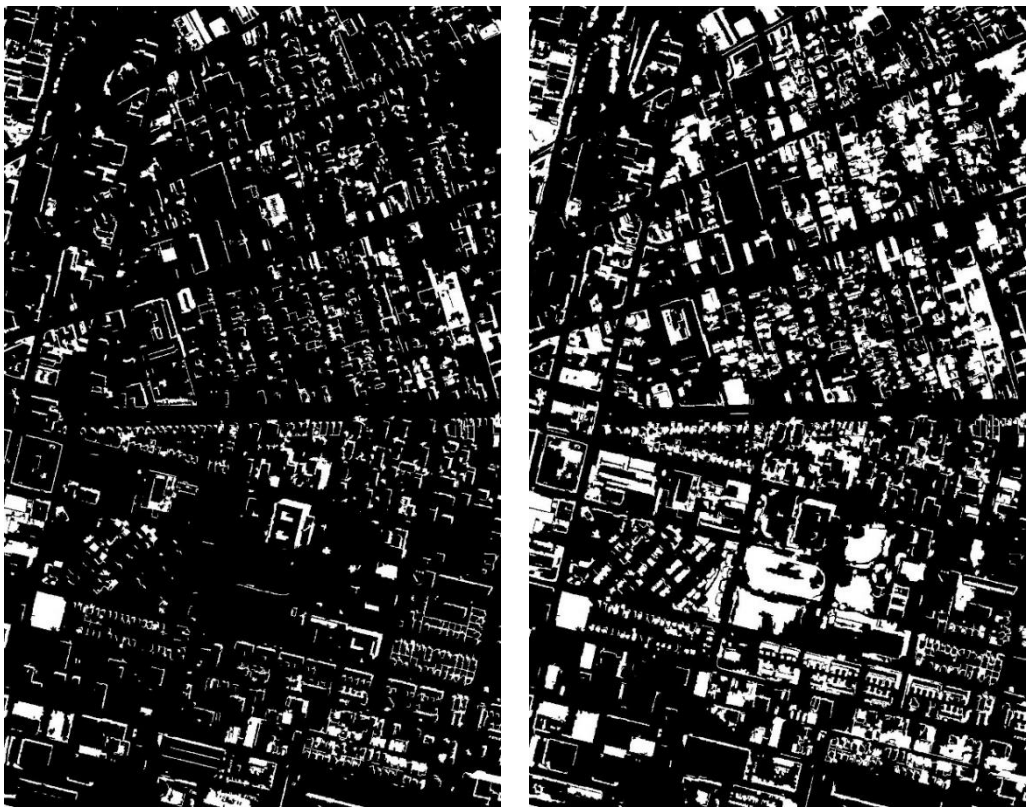

(c) (d)

**Figure 12.** Binary change maps by OTSU of (a) supervised MAD, (b) unsupervised MAD, (c) stack PCA, and (d) the binary change maps of post-classification, where the changed areas are white, and the unchanged areas are black.

The binary change maps of supervised MAD, unsupervised MAD, stack PCA by OTSU thresholding method, and the binary change maps of post-classification method are shown in Figure 12. By visual interpretation, it can be observed that supervised MAD detected less changed areas, while the other methods detected quite a lot of changes covering the whole scene. Post-classification directly compares class type between two corresponding independent classification results yielded by corresponding single sensor data. If the two class types are different, these areas will be determined as changed areas. Figure 12 (d) shows that the changed areas are much more than the unchanged areas, which is caused by the accumulation of independent classification errors in post-classification.

In order to carry out quantitative assessment, reference samples for change detection are selected as shown in Figure 13. The reference samples contain 9449 changed pixels shown as yellow, and 198842 unchanged pixels shown as green.

Peer-reviewed version available at Remote Sens. 2018, 10, 1349; doi:10.3390/rs10091349



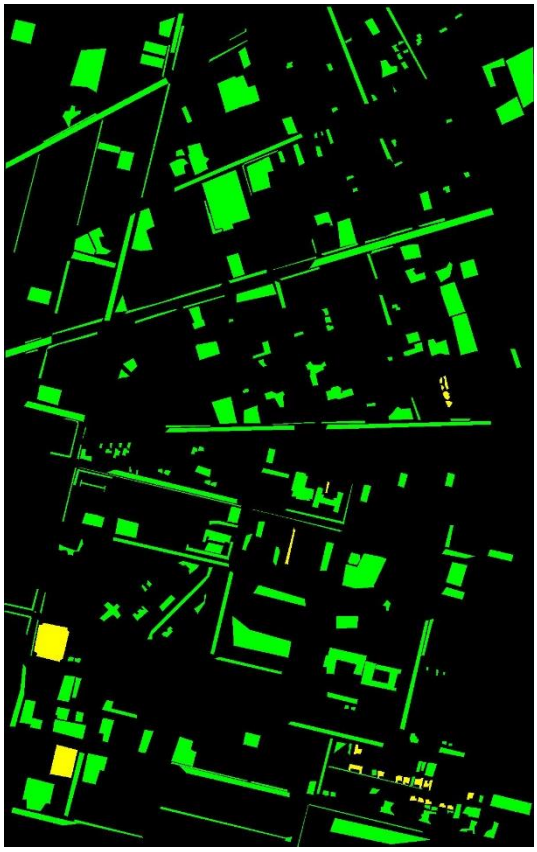

**Figure 13.** Reference samples for change detection, changed/unchanged samples are labelled in yellow/green color.

**Table 1.** Max kappa and current kappa for supervised MAD and comparative methods

| | Current Kappa | | |
|---|---|---|---|
| | K-means | OTSU | Max Kappa |
| sp_MAD | 0.5187 | 0.6419 | 0.7440 |
| un_MAD | 0.1901 | 0.2328 | 0.7550 |
| stack_PCA | 0.2003 | 0.2524 | 0.6881 |
| post-class | | | 0.1409 |

The quantitative evaluation is shown in Table 1. In order to reduce the influence of imbalance of training samples, we used Kappa coefficient. The max kappa coefficients, which can be obtained with all possible thresholds in the absolute image in Figure 10, are shown in the last column in the Table 1. The current kappa coefficients for the binary maps in Figure 12 are also shown in the middle column of Table 1. Two automatic thresholding methods are used in this paper, which are K-means clustering and OTSU thresholding.

It can be found that post-classification method got an extremely low accuracy, since the change detection accuracy is determined by the two independent classifications, and independent classifications only use single sensor data with a limited accuracy. Among all methods, unsupervised MAD can obtain the highest Max_Kappa, while supervised MAD can get obvious better performance after automatic thresholding. This is because supervised MAD can improve the separability of changed areas, thus the automatic thresholding method is easier to find the optimum threshold. Meanwhile, the thresholding method of OTSU outperforms K-means, and is selected as the input of change map in the following fusion process.

*4.2 Object-based Post-classification fusion*

In this paper, the main objective is to obtain the impervious surface distribution map for the newer target image considering landscape changes and observation differences. Therefore, the high resolution image in 2011 was used as the target image, and the LiDAR data in 2008 was used as the auxiliary data. For quantitative assessment, the reference maps for high resolution image in 2011 are produced by visual interpretation and shown in Figure 14. For test samples, roof samples are red with 62507 pixels, grass samples are green with 46923 pixels, road & parking lots samples are grey with 58337 pixels, soil are yellow with 22883 pixels, and pavement samples are cyan with 17440 pixels.

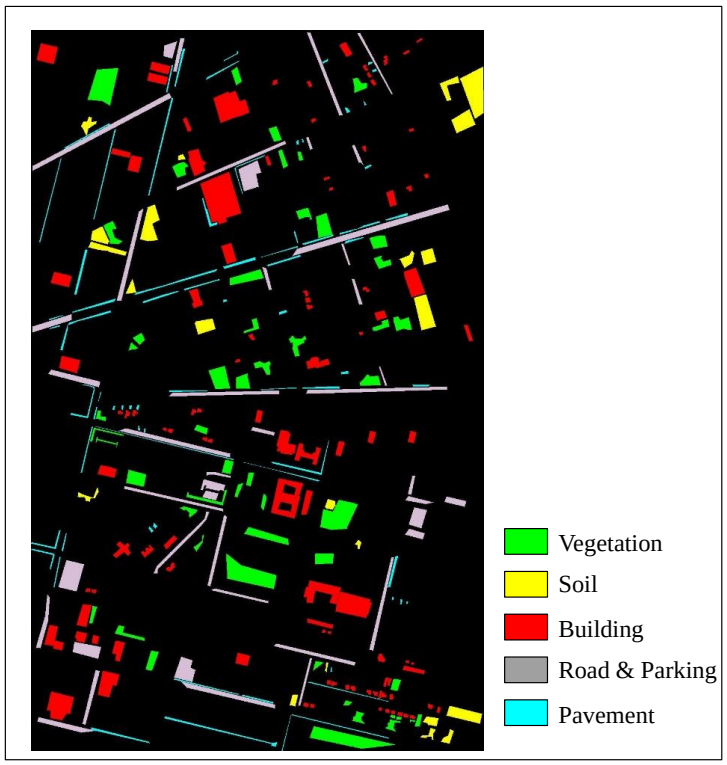


**Figure 14.** Reference map for the high resolution image in 2011

The classification results of independent classification, joint classification and the proposed method are shown in Figure 15. In order to obtain a better result, the segmentation scale is selected as 20 in the independent classifications of LiDAR data and high resolution image, while in the object-based post-classification fusion, the segmentation scale is selected as 10 for more homogeneous objects. In Figure 15 (a), the result of independent classification with high resolution image shows that the accuracy of building class is low with lots of misclassification errors. The independent classification result with LiDAR data in Figure 15 (b) illustrates that LiDAR data can classify the buildings with a good performance, while the pavement is hard to identified. Figure 15 (c) and (d) both show accurate classification maps, while the joint classification map contains shadow areas, which will be removed after the object-based post-classification fusion. Meanwhile, in some building areas, the result of joint classification shows obvious misclassifications of buildings, due to the no-data areas of LiDAR data. These problems are mostly corrected after the proposed object-based post-classification fusion steps.

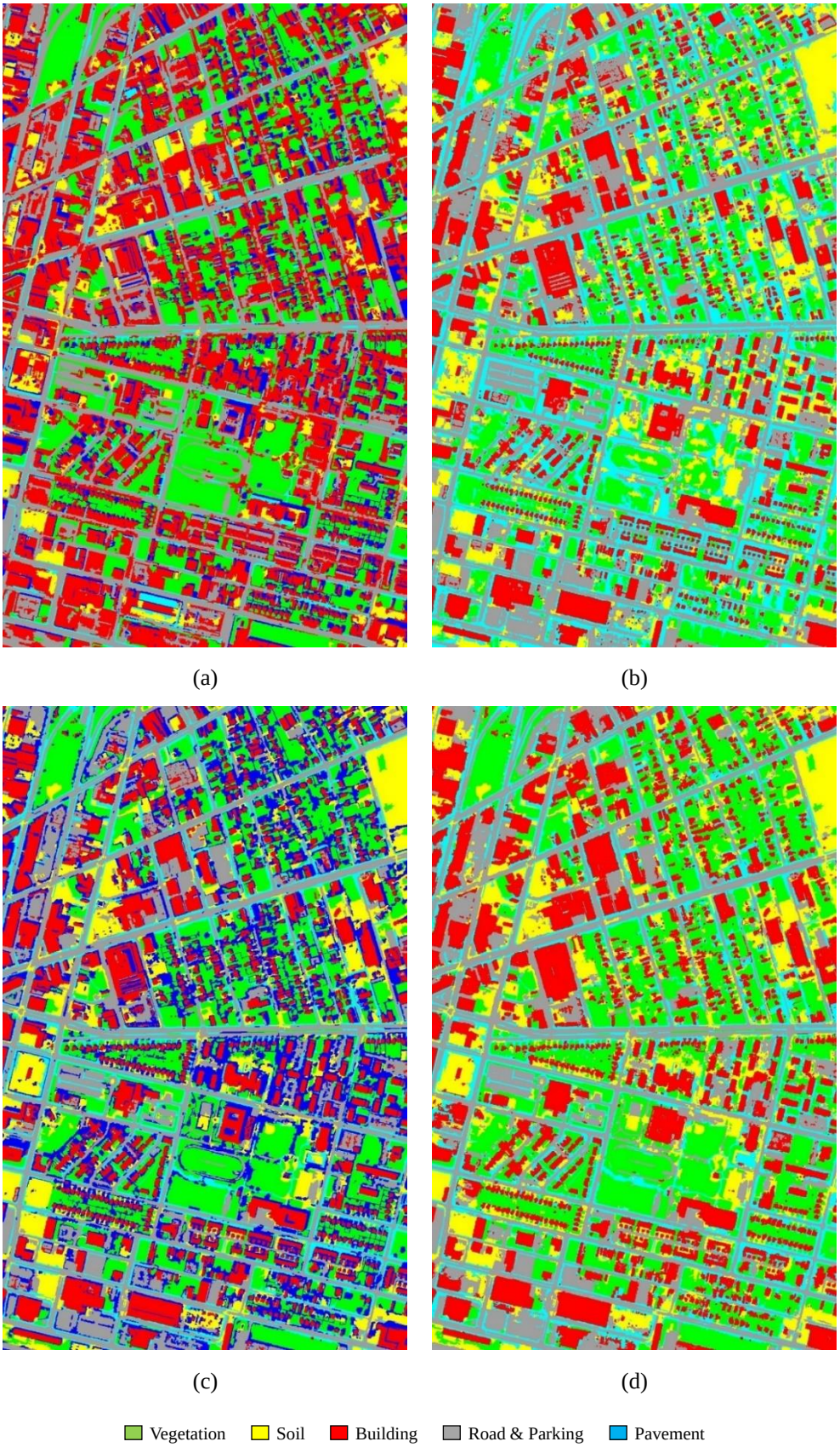


**Figure 15.** (a) independent classification map of high resolution image, (b) independent classification map of LiDAR data, (c) joint classification map with LIDAR data and high resolution image, and (d) classification map after the object-based post-classification fusion (the proposed method)

Table 2 shows the OAs and Kappa coefficients of classification maps for the proposed method and the comparative methods. It illustrates that the joint classification with both LiDAR data and high resolution image can obtain a better performance than each independent classification, while the proposed method can get an obvious improvement because it involves object-based post-classification fusion.

Table 3 shows the false alarm rate (FAR) [56] and omission rate (OR) of each class for the proposed method and the comparative methods. It can be observed that high resolution image cannot determine the building and soil accurately, while LiDAR data also get a bad performance in classifying soil and pavement. The joint classification with both high resolution image and LiDAR data got improvements in almost all classes compared with two independent classifications, which indicates the effectiveness of multi-sensor data classification. More importantly, the proposed method can get a further improvement compared with the joint classification, such as lower omission rate of building, and lower false alarm rate of soil. Therefore, the proposed method has the ability to obtain a higher classification accuracy, as shown in Table 2.

**Table 2.** Quantitative assessment of classification maps for the proposed method and the comparative methods

| | High resolution image | LiDAR data | Joint classification | The proposed method |
|---|---|---|---|---|
| OA(%) | 77.30 | 77.80 | 87.49 | **91.89** |
| KAPPA | 0.6999 | 0.7128 | 0.8372 | **0.8942** |

**Table 3.** False alarm rate (FAR) and omission rate (OR) of each class for the proposed method and the comparative method

| | High resolution image | | LiDAR data | | Joint classification | | The proposed method | |
|---|---|---|---|---|---|---|---|---|
| | FAR (%) | OR (%) | FAR (%) | OR (%) | FAR (%) | OR (%) | FAR (%) | OR (%) |
| Building | 31.13 | *26.68* | **3.36** | *24.23* | 3.75 | *19.82* | 5.00 | ***5.48*** |
| Vegetation | 0.50 | ***0.63*** | 10.97 | *23.63* | **0.39** | *1.83* | 1.10 | *1.96* |
| Soil | 39.39 | *44.22* | 30.53 | *23.24* | 28.11 | ***6.43*** | **5.01** | *13.87* |
| Pavement | **17.34** | *35.17* | 56.40 | *29.83* | 19.96 | *16.85* | 23.39 | ***7.11*** |
| Road & Parking | 26.48 | *24.39* | 25.32 | *16.17* | **19.22** | ***14.80*** | 21.91 | *16.09* |

Peer-reviewed version available at Remote Sens. 2018, 10, 1349; doi:10.3390/rs10091349



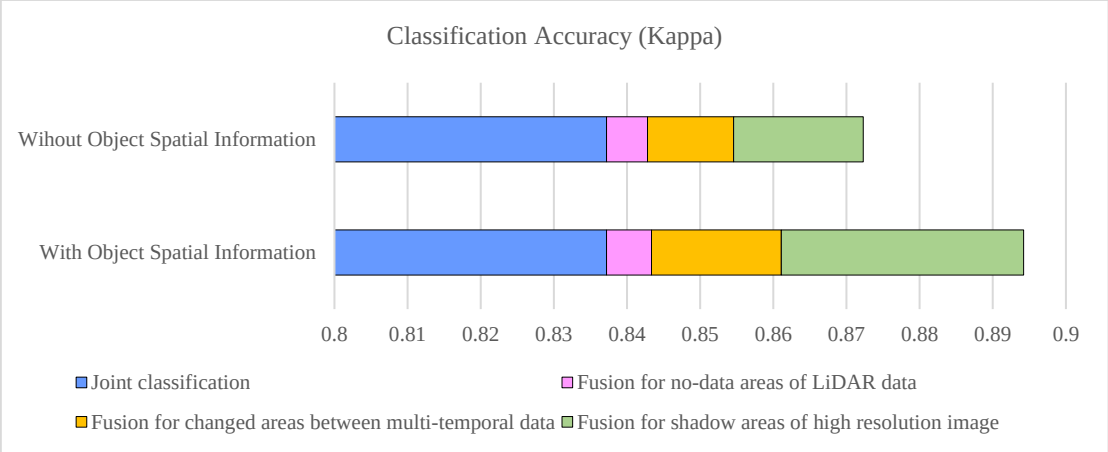


**Figure 16.** Classification accuracies with different fusion approaches

In order to test the proposed object-based post-classification fusion strategy, we compare two approaches to fuse the independent classification results and the joint classification result. One is to fill the no-data areas, changed areas and shadow areas with the corresponding independent classification result directly, without considering the object spatial information. For instance, the independent classification result provided by only high resolution image is used to fill the no-data areas in LiDAR data. The other one is to fuse the two independent classification results and the joint classification result considering the object spatial information through the proposed object-based post-classification fusion strategy, which is described in section 3.3. The bars in Figure 16 show the detailed improvement after each fusion step with or without object spatial information. Since there are three fusion steps after the joint classification results is obtained, different colors in Figure 16 indicate the increase of accuracy after each step. Figure 16 illustrates that all of the proposed three main fusion steps can improve the classification accuracy. Meanwhile, the fusion approach with the object spatial information has the ability to obtain a better performance than that without considering object spatial information. Therefore, the proposed fusion approach considering the object spatial information is effective in improving the performance of the final classification map.

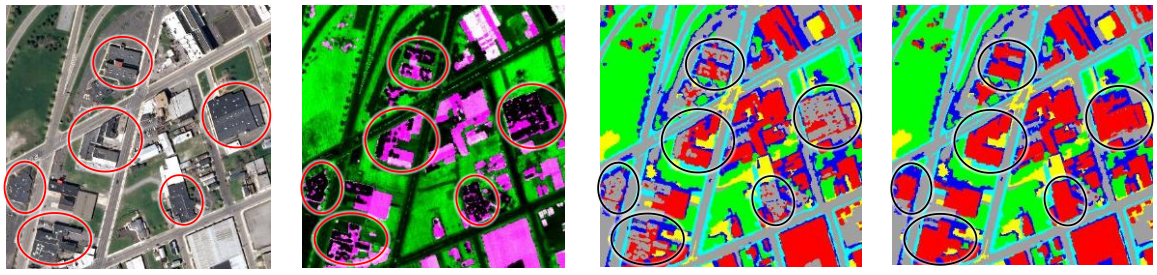

(a) (b) (c) (d)

**Figure 17.** Fusion for no-data areas of LiDAR data, which are (a) high resolution image, (b) LiDAR data, (c) joint classification map with LiDAR data and high resolution image before the object-based post-classification fusion, and (d) classification map after the object-based post-classification fusion.

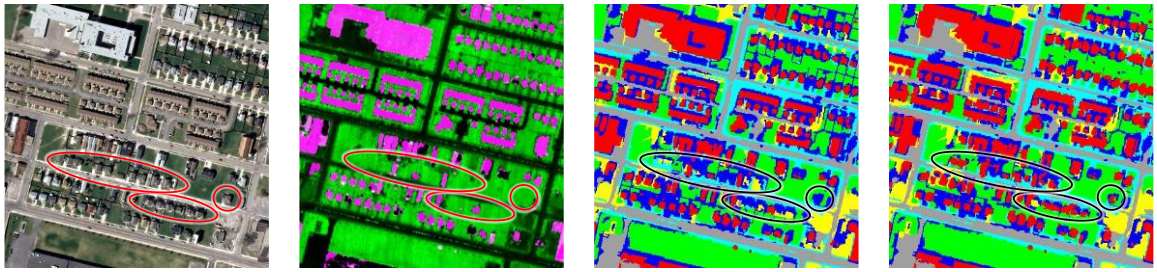

(a) (b) (c) (d)

**Figure 18.** Fusion for changed areas between multi-temporal data, which are (a) high resolution image, (b) LiDAR data, (c) joint classification map with LiDAR data and high resolution image before the object-based post-classification fusion, and (d) classification map after the object-based post-classification fusion.

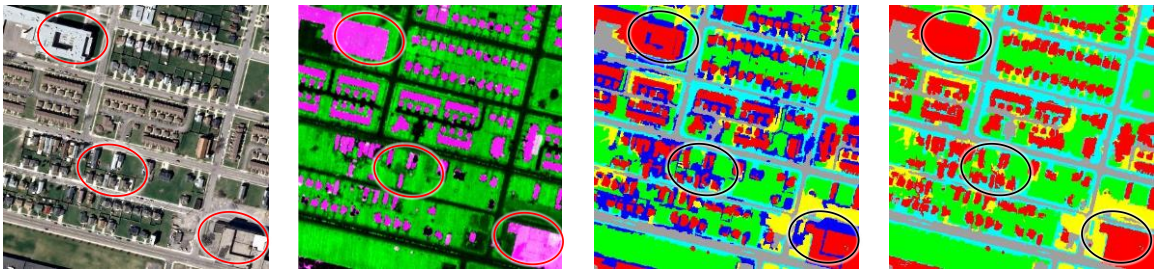

(a) (b) (c) (d)

**Figure 19.** Fusion for shadow areas of high resolution image, which are (a) high resolution image, (b) LiDAR data, (c) joint classification map with LiDAR data and high resolution image before the object-based post-classification fusion, and (d) classification map after the object-based post-classification fusion.

Figure 17, Figure 18, and Figure 19 show the improvements of each main step in the proposed object-based post-classification fusion method. In Figure 17, as shown in dark and red circles, there are many no-data areas for missing LiDAR data, which lead to obvious incorrect classification results. After the object-based post-classification fusion in Figure 17 (d), these areas are accurately corrected. Figure 18 shows the correction for changed areas, where there are obvious roof changes in the circles. Before correction, there areas are falsely classified. While after correction, the classification results in the corresponding areas are corrected as the building class, which is the right class in the newer high resolution image (the year of 2011). Figure 19 shows the correction in shadow areas. Since there are many shadows in high resolution image, the landscapes under shadows are hard to classified. With the proposed object-based post-classification fusion method, the landscape inside shadow areas can be identified with multi-sensor data.

Finally, the impervious surface distribution map is obtained by combining the corresponding landscapes, as shown in Figure 20, where the impervious surface is blue, and the pervious surface is green. The impervious surface contains building, road, parking lots, and pavement, while the others are pervious. It can be seen that the impervious surface distribution is very typical in American urban areas. Therefore, the impervious surface distribution mapping is extremely useful in the urban structure analysis, and the corresponding hydrology or city planning study.

## 5. Disscussion

### *5.1 Improvement over independent classification and joint classification*

For the detailed classification in the complex urban environment, it is hard to obtain a satisfactory accuracy with only single sensor data, such as single LiDAR data or only optical high resolution image. The reasons include: 1) the confusions between different landscapes in some observation information, such as the similar spectral values between roof and road, the similar density value between pavement and grass; 2) the disturbance in single sensor data, such as shadows in high resolution image, etc. The joint classification with the stacked LiDAR data and high resolution image utilize multi-sensor data, and makes use of abundant information from multiple physical characteristics. It can be seen in Table III that, compared with the independent classification, the joint classification lead to lower FARs and ORs for almost all the landscape classes. Especially, the joint classification got a very low FAR as that with LiDAR data, and very low FAR and OR as that with high resolution image. It indicates that the joint classification takes advantage of the information from multi-sensor data.

However, the joint classification with the multi-temporal stacked dataset ignores the real landscape changes and observation differences. The proposed method utilizes the joint classification as the basis, and employs three main steps of the object-based post-classification fusion for these data problems. Visually, the proposed object-based post-classification fusion can obviously correct the classification results, including: 1) the correction for the no-date areas as shown in Figure 17; 2) the correction for the changed areas as shown in Figure 18; and 3) the correction for the shadow areas as shown in Figure 19.

In quantitative assessment, if the landscape changes and observation differences are considered, even without the object spatial information, the classification accuracy (Kappa) can be improved from 0.8372 to 0.8723 as shown in Figure 16. With the proposed object-based post-classification fusion, the accuracy can be further improved to 0.8942. Figure 16 also illustrates that each fusion step works to solve the problems of landscape changes and observation differences. They obtain a step-by-step increase for the final classification accuracy.

For the detailed landscape classes shown in Table III, the proposed method obtains an obvious decrease of the OR of building class compared with the joint classification, since the no-data areas and shadow areas covering the buildings are corrected after the proposed fusion. The decrease of the FAR of soil class is mainly caused by the proposed fusion for no-date areas, since some of these areas are falsely classified as soil in joint classification. The obvious decrease of the OR of pavement class is due to the class re-identification under the shadows, since most pavements are beside the buildings and easily affected by the cast shadows.

Therefore, we can conclude that, it is necessary to consider the landscape changes and observation difference when mapping impervious surface with LiDAR data and high resolution image from difference acquisition time. The proposed method can obtain an obvious improvement compared with the joint classification.

### *5.2 Limitations*

The proposed method integrates the joint classification with the independent classifications according to the segmentation object maps. It is worth noting the improvement of the proposed method is mainly based on the joint classification. Thus, if the joint classification cannot provide an accurate class map, the accuracy of the improved result will also be limited. Besides, the proposed method makes use of the independent classification results, the segmentation object maps, the extraction of landscape changes and observation difference. Therefore, the error accumulation of all these processes will affect the performance of the proposed method.

When dealing with multi-sensor data, registration is one of the main pre-processing steps, which also included in our pre-processing part. Although the proposed method has the ability to extract some of the mis-registration areas by MAD change detection, it will contain lots of false alarms if the registration accuracy is quite low. Besides, the orthorectification of the high resolution image is also

Peer-reviewed version available at Remote Sens. 2018, 10, 1349; doi:10.3390/rs10091349



necessary to make the fusion with the LiDAR data. After orthorectification and accurate registration, slight mis-registration for high buildings can be handled by the proposed method.

### *5.3 Future Work*

Change detection between LiDAR data and high resolution image from different acquisition time is an important step to extract changed areas and mis-registration areas for fusion. In our future work, we want to develop a more accurate multi-sensor change detection method to detect changes between multi-temporal data.

In the proposed method, the joint classification is employed with the stacked LiDAR data and high resolution image. In order to better explore the complementary information, developing a new classification method with multi-sensor data is also one of the targets for our future work.

In the experiment, the landscape changes exist, but are not very common in the study site. In our future work, we want to collect LiDAR data and high resolution image covering the fast developing urban areas, such as cities in China. The effectiveness of the proposed method in the latest impervious surface mapping will be evaluated with LiDAR data and high resolution image covering these areas from different acquisition time, which contain obvious urban expansion and change in the study site.

## 6. Conclusion

Impervious surface mapping is very important for urban environment study, since it is an indicator for city development. Impervious surface mapping with multi-sensor data has been attracting increasing interest. However, when the multi-sensor data acquired at different times, some real landscape changes and observation differences between these data may exist, which will lead to unavoidable misclassification errors and decrease the final classification accuracy.

In this paper, we proposed an improved method for impervious surface mapping by considering landscape changes and observation differences between LiDAR data and high resolution image from different acquisition time. Multispectral high resolution image and LiDAR data in the Buffalo city are used in this study. The stacked data of high resolution image and LiDAR data was firstly segmented into object map with MRS algorithm to maintain the completeness of landscape in classification. And then supervised MAD and OTSU thresholding was used to detect data change by learning from the unchanged training samples. Finally, the core concept for the object-based post-classification fusion is proposed to take advantage of joint classification map with the stacked dataset and independent classification maps with the single sensor data. The object information is utilized during the fusion to keep the completeness of landscape object and improve the classification accuracy. After classification, the impervious surface map at newer time is conducted through the merge of roof, road, parking lots and pavement classes.

In the experiment, a study site in Buffalo was selected to prove the effectiveness of our proposed method. The real landscape changes, no-data areas in LiDAR data, mis-registration and shadow areas in high resolution image are the main problems. The experiment demonstrates that the supervised MAD method can get a better change detection results than post-classification change detection and other unsupervised methods. With the automatically obtained binary change detection result, the final land-cover maps by our proposed method show an obvious improvement compared with the joint classification and the independent classifications. Besides, the experiments indicate that the proposed object-based post-classification fusion considering the object spatial information can get a better performance than that by only filling the areas with independent classification results.

Our study demonstrates that it's necessary to consider landscape changes and observation differences in the fusion of LiDAR data and high resolution image from different acquisition time. With the development of multi-sensor remote sensing observation, our proposed method has the potentials to be used for detailed impervious surface mapping, updating, and real-time monitoring for urban environment with the newest single sensor data and historical different sensor data.

**Acknowledgments:** This work was supported by the National Natural Science Foundation of China under Grants 61601333, Natural Science Foundation of Hubei Province of China under Grants 2016CFB245, Open Research Fund of Key Laboratory of Digital Earth Science, Institute of Remote Sensing and Digital Earth, Chinese

Academy of Sciences under Grant 2017LDE003, Open Research Project of The Hubei Key Laboratory of Intelligent Geo-Information Processing KLIGIP-2017B05.

**Author Contributions:** Hui Luo had the original idea for this study, conducted experiments, and wrote the manuscript. Le Wang revised the manuscript and provided guidance on the overall research. Chen Wu provided some ideas about change detection method. Lei Zhang provided some revision comments for this manuscript.

**Conflicts of Interest:** The authors declare no conflict of interest.

## References


1. Arnold Jr, C.L.; Gibbons, C.J. Impervious surface coverage: The emergence of a key environmental indicator. *Journal of the American planning Association* **1996**, *62*, 243-258.
2. Hu, X.; Weng, Q. Impervious surface area extraction from ikonos imagery using an object-based fuzzy method. *Geocarto Int.* **2011**, *26*, 3-20.
3. Zhang, L.; Weng, Q. Annual dynamics of impervious surface in the pearl river delta, china, from 1988 to 2013, using time series landsat imagery. *ISPRS J. Photogramm.* **2016**, *113*, 86-96.
4. Weng, Q. Modeling urban growth effects on surface runoff with the integration of remote sensing and gis. *Environmental Management* **2001**, *28*, 737-748.
5. Weng, Q. Remote sensing of impervious surfaces in the urban areas: Requirements, methods, and trends. *Remote Sens. Environ.* **2012**, *117*, 34-49.
6. Hurd, J.D.; Civco, D.L. In *Temporal characterization of impervious surfaces for the state of connecticut*, ASPRS Annual Conference Proceedings, Denver, Colorado, May 2004, 2004; Denver, Colorado.
7. Harbor, J.M. A practical method for estimating the impact of land-use change on surface runoff, groundwater recharge and wetland hydrology. *Journal of the American Planning Association* **1994**, *60*, 95-108.
8. Yuan, F.; Bauer, M.E. Comparison of impervious surface area and normalized difference vegetation index as indicators of surface urban heat island effects in landsat imagery. *Remote Sens. Environ.* **2007**, *106*, 375-386.
9. Schueler, T.R. The importance of imperviousness. *Watershed protection techniques* **1994**, *1*, 100-111.
10. Xian, G.; Homer, C. Updating the 2001 national land cover database impervious surface products to 2006 using landsat imagery change detection methods. *Remote Sens. Environ.* **2010**, *114*, 1676-1686.
11. Wang, Q.; Meng, Z.; Li, X. Locality adaptive discriminant analysis for spectral-spatial classification of hyperspectral images. *IEEE Geosci. Remote Sens. Lett.* **2017**, *14*, 2077-2081.
12. Shi, C.; Wang, L. Linear spatial spectral mixture model. *IEEE Trans. Geosci. Remote Sens.* **2016**, *54*, 3599-3611.
13. Wang, Q.; Zhang, F.; Li, X. Optimal clustering framework for hyperspectral band selection. *IEEE Trans. Geosci. Remote Sens.* **2018**, 1-13.
14. Slonecker, E.T.; Jennings, D.B.; Garofalo, D. Remote sensing of impervious surfaces: A review. *Remote Sensing Reviews* **2001**, *20*, 227-255.
15. Shao, Z.; Liu, C. The integrated use of dmsp-ols nighttime light and modis data for monitoring large-scale impervious surface dynamics: A case study in the yangtze river delta. *Remote Sens.* **2014**, *6*, 9359-9378.
16. Deng, C.; Wu, C. A spatially adaptive spectral mixture analysis for mapping subpixel urban impervious surface distribution. *Remote Sens. Environ.* **2013**, *133*, 62-70.
17. Flanagan, M.; Civco, D.L. In *Subpixel impervious surface mapping*, Proceedings of the 2001 ASPRS Annual Convention, St. Louis, Missouri, USA, April, 2001, 2001; St. Louis, Missouri, USA.
18. Wu, C. Normalized spectral mixture analysis for monitoring urban composition using etm+ imagery. *Remote Sens. Environ.* **2004**, *93*, 480-492.
19. Lu, D.; Weng, Q. Use of impervious surface in urban land-use classification. *Remote Sens. Environ.* **2006**, *102*, 146-160.
20. Wu, C.; Murray, A.T. Estimating impervious surface distribution by spectral mixture analysis. *Remote Sens. Environ.* **2003**, *84*, 493-505.
21. Zhou, Y.; Wang, Y.Q. Extraction of impervious surface areas from high spatial resolution imagery by multiple agent segmentation and classification. *Photogramm. Eng. Remote Sens.* **2008**, *74*, 857-868.

22. Yuan, F.; Bauer, M.E. In *Mapping impervious surface area using high resolution imagery: A comparison of object-based and per pixel classification*, American society for photogrammetry and remote sensing annual conference proceedings, Reno, Nevada, 2006.
23. Li, P.J.; Guo, J.C.; Song, B.Q.; Xiao, X.B. A multilevel hierarchical image segmentation method for urban impervious surface mapping using very high resolution imagery. *IEEE J. Sel. Topics. Appl. Earth Observ. Remote Sens.* **2011**, *4*, 103-116.
24. Huang, X.; Zhang, L.; Gong, W. Information fusion of aerial images and lidar data in urban areas: Vector-stacking, re-classification and post-processing approaches. *Int. J. Remote Sens.* **2011**, *32*, 69-84.
25. Yan, W.Y.; Shaker, A.; El-Ashmawy, N. Urban land cover classification using airborne lidar data: A review. *Remote Sens. Environ.* **2015**, *158*, 295-310.
26. Zhang, J.; Lin, X. Advances in fusion of optical imagery and lidar point cloud applied to photogrammetry and remote sensing. *International Journal of Image and Data Fusion* **2017**, *8*, 1-31.
27. Zhang, J. Multi-source remote sensing data fusion: Status and trends. *International Journal of Image and Data Fusion* **2010**, *1*, 5-24.
28. Guo, T.; Yasuoka, Y. In *Snake-based approach for building extraction from high-resolution satellite images and height data in urban areas*, Proceedings of the 23rd Asian Conference on Remote Sensing, 2002; pp 25-29.
29. Wang, R. 3d building modeling using images and lidar: A review. *International Journal of Image and Data Fusion* **2013**, *4*, 273-292.
30. Meng, X.; Wang, L.; Silván-Cárdenas, J.L.; Currit, N. A multi-directional ground filtering algorithm for airborne lidar. *ISPRS J. Photogramm.* **2009**, *64*, 117-124.
31. Guo, B.; Huang, X.; Zhang, F.; Sohn, G. Classification of airborne laser scanning data using jointboost. *ISPRS J. Photogramm.* **2015**, *100*, 71-83.
32. Lafarge, F.; Descombes, X.; Zerubia, J.; Pierrot-Deseilligny, M. Automatic building extraction from dems using an object approach and application to the 3d-city modeling. *ISPRS J. Photogramm.* **2008**, *63*, 365-381.
33. Yang, B.; Dong, Z.; Zhao, G.; Dai, W. Hierarchical extraction of urban objects from mobile laser scanning data. *ISPRS J. Photogramm.* **2015**, *99*, 45-57.
34. Zhou, W.; Troy, A. An object-oriented approach for analysing and characterizing urban landscape at the parcel level. *Int. J. Remote Sens.* **2008**, *29*, 3119-3135.
35. Guo, L.; Chehata, N.; Mallet, C.; Boukir, S. Relevance of airborne lidar and multispectral image data for urban scene classification using random forests. *ISPRS J. Photogramm.* **2011**, *66*, 56-66.
36. Zhou, W. An object-based approach for urban land cover classification: Integrating lidar height and intensity data. *IEEE Geoscience and Remote Sensing Letters* **2013**, *10*, 928-931.
37. Hodgson, M.E.; Jensen, J.R.; Tullis, J.A.; Riordan, K.D.; Archer, C.M. Synergistic use of lidar and color aerial photography for mapping urban parcel imperviousness. *Photogramm. Eng. Remote Sens.* **2003**, *69*, 973-980.
38. Im, J.; Lu, Z.Y.; Rhee, J.; Quackenbush, L.J. Impervious surface quantification using a synthesis of artificial immune networks and decision/regression trees from multi-sensor data. *Remote Sens. Environ.* **2012**, *117*, 102-113.
39. Hartfield, K.A.; Landau, K.I.; Leeuwen, W.J.D.v. Fusion of high resolution aerial multispectral and lidar data: Land cover in the context of urban mosquito habitat. *Remote Sens.* **2011**, *3*, 2364.
40. Yu, B.; Liu, H.; Zhang, L.; Wu, J. In *An object-based two-stage method for a detailed classification of urban landscape components by integrating airborne lidar and color infrared image data: A case study of downtown houston*, Urban Remote Sensing Event, 2009 Joint, 2009; IEEE: pp 1-8.
41. Benz, U.C.; Hofmann, P.; Willhauck, G.; Lingenfelder, I.; Heynen, M. Multi-resolution, object-oriented fuzzy analysis of remote sensing data for gis-ready information. *ISPRS J. Photogramm.* **2004**, *58*, 239-258.
42. Nielsen, A.A.; Conradsen, K.; Simpson, J.J. Multivariate alteration detection (mad) and maf postprocessing in multispectral, bitemporal image data: New approaches to change detection studies. *Remote Sens. Environ.* **1998**, *64*, 1-19.
43. Canty, M.J.; Nielsen, A.A. Automatic radiometric normalization of multitemporal satellite imagery with the iteratively re-weighted mad transformation. *Remote Sens. Environ.* **2008**, *112*, 1025-1036.
44. Nielsen, A.A. The regularized iteratively reweighted mad method for change detection in multi- and hyperspectral data. *IEEE Trans. Image Process.* **2007**, *16*, 463-478.
45. Otsu, N. A threshold selection method from gray-level histograms. *Automatica* **1975**, *11*, 23-27.
46. Wu, C.; Zhang, L.; Du, B. Kernel slow feature analysis for scene change detection. *IEEE Trans. Geosci. Remote Sens.* **2017**, *55*, 2367-2384.

47. Wu, C.; Du, B.; Cui, X.; Zhang, L. A post-classification change detection method based on iterative slow feature analysis and bayesian soft fusion. *Remote Sens. Environ.* **2017**, *199*, 241-255.
48. Coppin, P.; Jonckheere, I.; Nackaerts, K.; Muys, B.; Lambin, E. Digital change detection methods in ecosystem monitoring: A review. *Int. J. Remote Sens.* **2004**, *25*, 1565-1596.
49. Lu, D.; Mausel, P.; Brondizio, E.; Moran, E. Change detection techniques. *Int. J. Remote Sens.* **2004**, *25*, 2365-2401.
50. Singh, A. Review article digital change detection techniques using remotely-sensed data. *Int. J. Remote Sens.* **1989**, *10*, 989-1003.
51. Zhou, W.; Huang, G.; Troy, A.; Cadenasso, M. Object-based land cover classification of shaded areas in high spatial resolution imagery of urban areas: A comparison study. *Remote Sens. Environ.* **2009**, *113*, 1769-1777.
52. Definiens. Definiens professional 5 reference book. Definiens: München, 2006.
53. Suykens, J.A.K.; Vandewalle, J. Least squares support vector machine classifiers. *Neural Processing Letters* **1999**, *9*, 293-300.
54. Collins, J.B.; Woodcock, C.E. An assessment of several linear change detection techniques for mapping forest mortality using multitemporal landsat tm data. *Remote Sens. Environ.* **1996**, *56*, 66-77.
55. Li, H.; Xiao, P.; Feng, X.; Yang, Y.; Wang, L.; Zhang, W.; Wang, X.; Feng, W.; Chang, X. Using land long-term data records to map land cover changes in china over 1981-2010. *IEEE J. Sel. Topics. Appl. Earth Observ. Remote Sens.* **2017**, *10*, 1372-1389.
56. Wu, C.; Du, B.; Zhang, L. A subspace-based change detection method for hyperspectral images. *IEEE J. Sel. Topics. Appl. Earth Observ. Remote Sens.* **2013**, *6*, 815-830.